POLITECNICO DI TORINO
Repository ISTITUZIONALE

Gradient-based image generation for thermographic material inspection

*Original*
Gradient-based image generation for thermographic material inspection / Razza, V., Santoro, L., De Maddis, M.. - In: APPLIED THERMAL ENGINEERING. - ISSN 1359-4311. - (2025). [10.1016/j.applthermaleng.2025.125900]

*Availability:*
This version is available at: 11583/2997621 since: 2025-02-19T15:06:10Z

*Publisher:*
Elsevier

*Published*
DOI:10.1016/j.applthermaleng.2025.125900

*Terms of use:*

This article is made available under terms and conditions as specified in the corresponding bibliographic description in the repository

*Publisher copyright*

(Article begins on next page)

13 November 2026

Applied Thermal Engineering 268 (2025) 125900

Contents lists available at ScienceDirect

Applied Thermal Engineering

journal homepage: www.elsevier.com/locate/ate

Research paper

# Gradient-based image generation for thermographic material inspection

Valentino Razza [a,*], Luca Santoro [b], Manuela De Maddis [a]

[a] Department of Management and Production Engineering, Politecnico di Torino, 10129 Torino, Italy
[b] Department of Mechanical and Aerospace Engineering, Politecnico di Torino, 10129 Torino, Italy

ARTICLE INFO

*Keywords:*
Thermography
Signal analysis
Non-destructive testing

ABSTRACT

Infrared thermography is a non-contact, cost-effective, and non-destructive technique for defect inspection. Analyzing the surface temperature behavior of an object excited by a suitably designed heat source provides information on the internal structure of the object. The thermal diffusion coefficient of the material is the main physical parameter determining the surface temperature profile. Defects are typically characterized by a different thermal diffusion coefficient than the base material, leading to changes in the heat transfer model.

If defect identification from thermography analysis is possible and computationally efficient, interpreting the results often requires trained users. In this work, we propose an algorithm for active thermography data analysis that generates images enabling the detection of the position and size of internal defects. Experimental results validate the approach, showing its ability to detect blind flat-top holes of 3 mm diameter and depths of 0.5 mm and 0.8 mm in a 1 mm thick DP600 steel plate. In addition, tests of the proposed technique show promising results in highlighting embedded defects in a 3D-printed polylactic acid object, proving the algorithm efficacy for the inspection of materials with different heat diffusion coefficients. These findings highlight the robustness and practicality of the proposed method for industrial applications.

## 1. Introduction

Nondestructive testing (NDT) ensures the structural integrity and safety of components used in various industries, such as aerospace, automotive, construction, and energy. NDT techniques allow for the evaluation of material properties and the detection of defects without compromising the functionality or serviceability of the component. Defects can be identified using a probing energy source and evaluating the physical material properties.

Established NDT methods include ultrasonic testing (UT), which utilizes sound waves to identify internal flaws, and X-ray radiography, which employs penetrating radiation to visualize internal structures. These methods have been widely used for decades to inspect metallic and polymeric components. However, each method has its limitations. For instance, UT requires physical contact with the sample and a couplant for sound wave transmission, which may not be suitable for all materials or geometries. X-ray radiography necessitates exposure to ionizing radiation, raising safety concerns and requiring strict regulatory compliance.

Infrared thermography has emerged as a versatile NDT technique that offers several advantages over traditional methods. It is a non-contact method that allows for rapid data acquisition and applies to a wide range of materials, including metals and polymers [1–3]. Thermography detects surface temperature variations, which can be indicative of subsurface defects such as cracks, delaminations, inclusions, corrosion, and fatigue damage (see, e.g., [4–6]). Unlike some NDT methods that may be limited by material properties or defect orientation, thermography can often provide valuable insights regardless of these factors.

The key advantages of thermography include its non-contact nature, which eliminates the need for surface preparation and reduces safety hazards associated with radiation exposure [7]. Thermographic cameras allow for rapid data acquisition, enabling significantly faster inspection times compared to some traditional NDT methods. This enhanced speed is crucial in high-volume production lines or time-sensitive maintenance scenarios where efficiency is paramount. Additionally, thermography is highly versatile and can be applied to various materials, including metals and polymers, and to detect a wide range of defects. This versatility can reduce the need for multiple specialized NDT methods, leading to overall cost savings.

In thermography, two primary techniques are used to analyze temperature variations within objects: passive and active thermography. Passive thermography relies solely on the natural infrared radiation emitted by the object itself. This inherent thermal signature is captured by an infrared camera, allowing for the visualization of temperature differentials across the object's surface. The simplicity of this method

* Corresponding author.
*E-mail addresses:* valentino.razza@polito.it (V. Razza), luca.santoro@polito.it (L. Santoro), manuela.demaddis@polito.it (M.D. Maddis).

https://doi.org/10.1016/j.applthermaleng.2025.125900
Received 18 October 2024; Received in revised form 5 February 2025; Accepted 9 February 2025
Available online 18 February 2025
1359-4311/© 2025 The Authors. Published by Elsevier Ltd. This is an open access article under the CC BY-NC-ND license (http://creativecommons.org/licenses/by-nc-nd/4.0/).

makes it well-suited for applications where manipulating the environment is impractical or undesirable. Passive thermography finds applications in building inspections to identify heat loss [8,9], predictive maintenance in electrical equipment [10,11], search-and-rescue operations to locate individuals [12], and medical diagnostics for fever detection [13]. Moreover, passive thermography is helpful in chemical applications, where temperature analysis improves the fatigue analysis without probes that may interact with the reactions [14].

Conversely, active thermography employs an external energy source, such as high-intensity lamps or lasers, to induce thermal excitation within the object. This controlled heating amplifies pre-existing temperature variations, leading to a more pronounced thermal contrast in the captured image. The enhanced sensitivity detects subtle defects, such as cracks [15] or material delamination [16]. Active thermography is particularly valuable in industrial settings for non-destructive testing [17,18] and preventive maintenance procedures [19]. Moreover, active thermography finds application in laboratory testing for material characterization [20–22].

Techniques such as finite element analysis (FEA) offer insights into the thermal behavior of materials with defects under controlled conditions. FEA can be used to optimize test parameters, such as the heat source modulation frequency in active thermography, to improve defect detection in both metallic and polymeric materials [2,3].

It is essential to acknowledge that thermography also has limitations. Factors like surface condition, material properties, and the specific defect type can influence defect detection effectiveness. First, contactless temperature measurement requires knowledge about the radiation source, like the object emissivity that may change across the thermal camera frame. In [23], the authors propose a fuzzy logic to improve the temperature estimation. Additionally, quantitative analysis of defect depth may require more advanced techniques or complementary NDT methods for confirmation. Moreover, interpreting thermographic data often poses challenges; the results can be complex to analyze, requiring specialized training for users to identify defects and operate the system effectively. However, the advantages of thermography, including its safety, speed, versatility, and real-time monitoring capabilities, make it a valuable asset in the NDT toolbox for inspecting either metallic or polymeric components [24].

In the literature, several approaches are proposed to analyze thermographic data. In passive thermography, the analysis is often performed by comparing the infrared data to a baseline value [25]. For example, colder or hotter areas denote heat losses in building inspection. Electronic circuits are also well inspected through passive thermography since defects increase resistance, leading to higher localized temperatures than normal operating ones (see, e.g., [26,27]).

In active thermography, algorithms are often categorized based on the excitation type. In pulsed thermography, the sample is excited by a single heat pulse, and the transient behavior is analyzed [28–30]. Lock-in thermography uses a sinusoidal heat source, and the analysis is performed by evaluating the stationary input–output delay, given an external time reference generator (see, e.g., [31]). More recently, machine-learning techniques have been applied to infrared data. Typically, the algorithm aims to classify defects through a neural network. In [32], a fault classification algorithm from passive thermography data is proposed, where the infrared video is preprocessed to extract features representing the neural network inputs. In [33], a passive thermography algorithm based on a Deep Convolutional Neural Network (DCNN) that integrates other sensor information is used to diagnose faults. One of the main drawbacks of neural network-based algorithms is the training phase, which requires a large amount of data suitably labeled with the defects to be identified.

In this work, we propose a novel algorithm for material inspection based on active thermography. We highlight the defects as differences from the nominal case by evaluating the heat transfer behavior. Our method generates easily interpretable images from active thermography data, enabling even non-expert users to quickly and precisely assess the presence of defects without extensive training. Active thermography is chosen for the flexibility of the excitation method, allowing it to be adapted to the particular object to be analyzed. Here, we use a modulated laser as a heat source; however, the same results apply to other heat sources like infrared lamps. This work considers the heat source acting with a generic periodic signal at a given frequency. Fourier transform is used to extract features from the infrared video. The output feature considered is the through-plane phase delay, which is shown to behave as a smooth function in nominal conditions, i.e., a uniform semi-infinite specimen. Defects act as obstacles for the heat waves propagating internally to the material, leading to surface-localized variations from the nominal case in the extracted feature. We evaluate the through-phase gradient to generate a gray-scale image that highlights the internal defects. The proposed algorithm generalizes the lock-in thermography inspection since we consider a generic heat input function shape, and the through-plane phase is only one possible feature to extract. The algorithm has low computational complexity because it relies on the discrete Fourier transform, whose efficient implementations are well-known in the literature (see, e.g., [34]). This work extends our previous results in [35,36], where a similar approach has been used to detect the size of the weld diameter in resistance spot welding joints.

The remainder of the paper is organized as follows. Section 2 recalls the heat transfer model, while Section 3 provides test cases in thermal processes where our approach finds application. Section 4 describes the proposed algorithm and Section 5 shows the effectiveness of the proposed methodology through calibration tests. Conclusions and final remarks end the paper.

## 2. Background

This work proposes a sample analysis method through an active thermography setup. The sample under test is thermally exited through a laser, and a thermal camera acquires the temperature profile. The thermal profile can be acquired on the opposite side, i.e., in transmission mode (Fig. 1 shows the experimental setup used, while the conceptual schema is given in Fig. 2), or on the same side excited by the laser, i.e., in reflection mode. This setup is portable and can be installed in industrial systems, such as welding robots, to control resistance spot welds automatically. The industrial interest in active thermography as an NDT method led to some commercial solutions, like the one proposed by InfraTec GmbH [37], where the heat source is an infrared lamp.

The heat source is assumed circular with a radius $a$, whose shape applies generically to the most common sources, i.e., laser and infrared lamps. The experiments are performed by ensuring a constant ambient temperature for the duration of the single test, and the specimen is thermally excited through a pulsed laser source. The theoretical thermal behavior acquired from the thermal camera can be computed under some hypothesis.

We recall the heat transfer model across a semi-infinite uniform slab of thickness $\ell$. The nominal laser power has a Gaussian distribution over a spot of radius $a$. The specimen absorbed laser power is

$$P(\rho,t)=\eta\frac{P_o(t)}{\pi a^2}e^{-2\rho^2/a^2}, \tag{1}$$

where $\rho$ is the distance from the center of the laser spot, $P_o(t)$ is the heating temporal profile, and $\eta$ is the absorbed power fraction. The heat conduction equation through a uniform medium is described by

$$\frac{\partial^2\tau_i}{\partial\rho^2}+\frac{1}{\rho}\frac{\partial\tau_i}{\partial\rho}+\frac{\partial^2\tau_i}{\partial z^2}=\frac{1}{D_i}\frac{\partial\tau_i}{\partial t}, \tag{2}$$

where $\tau_i(\rho,z,t)=T_i(\rho,z,t)-T_0$ is the temperature difference from the initial value $T_0$ in the region $i$, and $D_i$ is the diffusion coefficient. Eq. (2) is subjected to the boundary conditions along $z$ surfaces

$$\tau_{e1}(\rho,0,t)=\tau_s(\rho,0,t) \tag{3a}$$

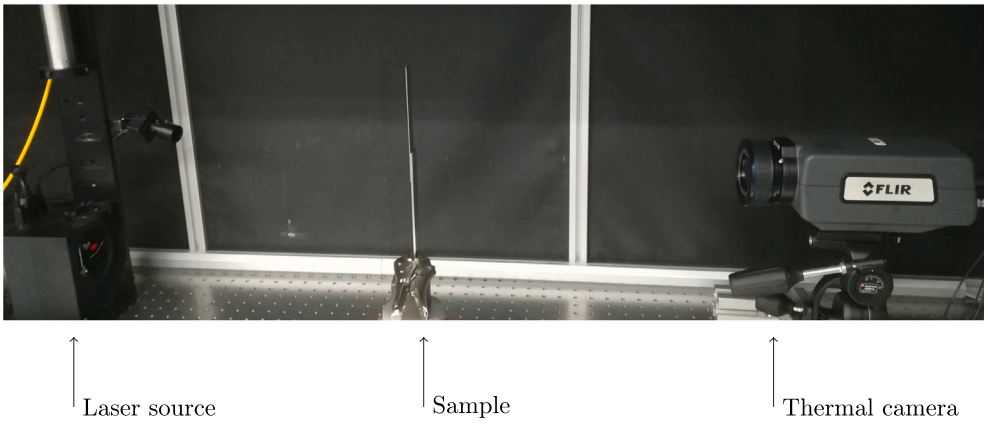


**Fig. 1.** Active thermography experimental setup in transmission mode.

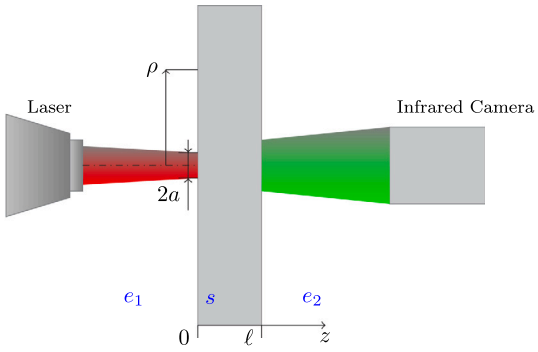


**Fig. 2.** Cross-section of the experimental setup and the reference system for the transmission mode setup. The laser excites one side of the specimen, while the infrared camera acquires the rear sample temperature.

$$\tau_{e2}(\rho,\ell,t) = \tau_s(\rho,\ell,t) \tag{3b}$$

where subscripts $e1$ and $e2$ denote the air regions for $z \le 0$ and $z \ge \ell$, respectively, and subscript $s$ denotes the sample, i.e., $0 \le z \le \ell$. Moreover, by assuming a sufficiently short observation period, the temperature within all of the regions does not change for a sufficiently large distance from the laser spot, i.e.,

$$\lim_{\rho\to\infty} \tau_i(\rho,z,t) = 0 \tag{4}$$

as well as the air temperature is constant far from the sample

$$\lim_{z\to-\infty} \tau_{e1}(\rho,z,t) = \lim_{z\to+\infty} \tau_{e2}(\rho,z,t) = 0. \tag{5}$$

In addition, the heat transfer equilibrium along the surfaces, by convection and radiation, leads to the following relationships

$$-K_s \left.\frac{\partial \tau_s}{\partial z}\right|_{z=0} = -K_e \left.\frac{\partial \tau_{e1}}{\partial z}\right|_{z=0} + h\tau_s|_{z=0} - P(\rho,t), \tag{6a}$$

$$-K_s \left.\frac{\partial \tau_s}{\partial z}\right|_{z=\ell} = -K_e \left.\frac{\partial \tau_{e2}}{\partial z}\right|_{z=\ell} - h\tau_s|_{z=\ell}, \tag{6b}$$

where $h$ is the heat transfer coefficient, and $K_e$ and $K_s$ are the air and sample thermal conductivity, respectively.

We rewrite the thermal behavior $\tau_i(\rho,z,t)$ into the spatial–temporal frequency domain by applying the Laplace and the Hankel transforms (see, e.g., [38]), i.e.,

$$\overline{T}_i(\delta,z,s) = \int_0^\infty \int_0^\infty \delta J_0(\delta\rho)\tau_i(\rho,z,t)e^{-st}dt\, d\rho \tag{7}$$

where $\delta$ is the Hankel variable, $J_0(\delta\rho)$ is the 0th order Bessel function, and $s$ is the Laplace complex variable. Given (7) and (2), the following relation hold

$$\frac{d^2}{dz^2}\overline{T}_i(\delta,z,s) - \left(\delta^2 + \frac{s}{D_i}\right)\overline{T}_i(\delta,z,s) = 0. \tag{8}$$

The sample temperature profiles can be computed through the inverse of the transform (7) and considering the conditions (3a)–(6), i.e.,

$$\tau_s(\rho,z,t) = \int_{\sigma-i\omega}^{\sigma-i\omega} \int_0^\infty \delta J_0(\delta\rho)\overline{T}_s(\delta,z,s)d\delta\, ds, \tag{9}$$

where

$$\overline{T}_s(\delta,z,s) = \frac{\eta}{4\pi} P_o(s) e^{-(\delta a)^2/8} \frac{Ae^{-\beta_s(z-\ell)} + Be^{\beta_s(z-\ell)}}{A^2e^{\beta_s\ell} - B^2e^{-\beta_s\ell}}, \tag{10}$$

$A = K_s\beta_s + K_e\beta_e + h$, $B = K_s\beta_s - K_e\beta_e - h$, $\beta_i^2 = \delta^2 + s/D_i$, $i = \{e,s\}$, and $P_o(s)$ is the Laplace transform of $P_o(t)$.

From (10), the oscillation component of $\tau_s$ at frequency $\omega_\ell = 2\pi f_\ell$ is given by

$$\tilde{\tau}_s(\rho,z) = \int_0^\infty \delta J_0(\delta\rho)\overline{T}_s(\delta,z,j\omega_\ell)d\delta. \tag{11}$$

Eq. (11) has no analytical expression, but it must be evaluated through numerical simulations. It is worth noting that the ratio

$$G(\rho,z) = \frac{\tilde{\tau}_s(\rho,z)}{P_o(j\omega_\ell)} \tag{12}$$

represents the transfer function value evaluated for the specific frequency $\omega_\ell$, as a function of the cylindrical coordinates $(\rho,z)$. Here, we focus on the transfer function phase, $\phi(\rho,z) = \angle G(\rho,z)$, since the module is affected by large measurement uncertainty (see, e.g., [35]).

**Remark 1.** Contactless temperature measurement systems, such as infrared cameras, rely on the thermal radiation emitted by the object. The Stefan–Boltzmann law relates the thermal radiation $M$ with the temperature $T$ as

$$M = \varepsilon\sigma T^4 \tag{13}$$

where $\sigma$ is the Stefan–Boltzmann constant and $0 \le \varepsilon \le 1$ is the emissivity. The exact $\varepsilon$ value depends on the surface chemical composition and geometrical structure. The surface color, roughness, and temperature influence the value of $\varepsilon$, leading to large uncertainties in the absolute temperature measurement. Thus, while evaluating (11), the module $|G(\rho,z)|$ typically includes superficial defects, like scratches and object shapes. On the other hand, the transfer function phase $\phi(\rho,z)$ measures the input–output signal response delay, which is less influenced by $\varepsilon$.

**Remark 2.** It is worth noting that, in this work, we consider a laser as the heat source. However, the results in (12) apply to a generic input, given a cylindrical symmetry. For example, the laser could be replaced by an infrared lamp, heating a region of radius $a$. The user can choose between a laser or an infrared lamp based on needs, like the testing surface area and the required irradiated power.

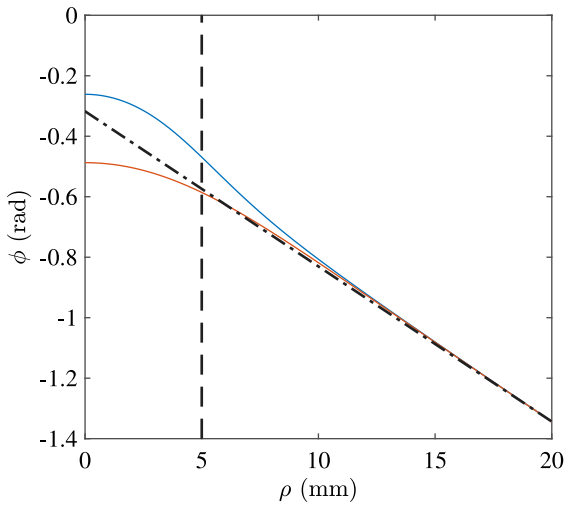


**Fig. 3.** Example of laser-thermal signal delay $\angle G(\rho, z)$ in transmission (red) and reflection (blue) mode. The vertical dashed line highlights the laser spot radius $a$, and the oblique dash-dotted line is the asymptotical behavior.

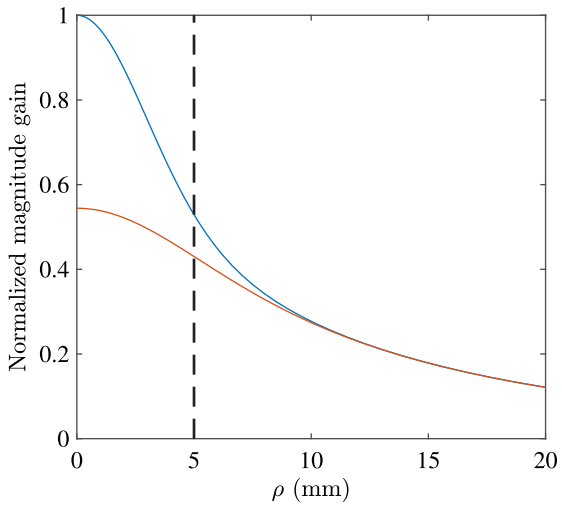


**Fig. 4.** Example of laser-thermal heat gain $|G(\rho, z)|$ in transmission (red) and reflection (blue) mode. The vertical dashed line highlights the laser spot radius $a$. The gain behaviors are normalized to the maximum achieved in reflection mode.

In [20], the transmission mode delay is numerically evaluated for a small laser spot radius $a$ value, leading to

$$\phi(\rho, \ell) = \phi_0(\omega_\ell) - \frac{\rho}{\lambda}, \text{ for } \rho \gg a, \tag{14}$$

where

$$\lambda = \sqrt{2D_s/\omega_\ell} \tag{15}$$

is the thermal diffusion length, and $\phi_0$ is a phase lag constant value that depends on slab thickness, modulation frequency, and laser to temperature acquisition system delay. In this work, we are interested in the phase delay while using a larger laser spot and evaluating the thermal phase delay in both reflection and transmission modes. Fig. 3 shows the laser to thermal signal delay, numerically evaluated from (11). While the numerical results depend on the specific parameter values considered for the simulation, some general considerations can be drawn. The simulation results, depicted in Figs. 3 and 4, have been computed by considering a laser radius of $a = 5$ mm, exciting an aluminum plate with a thickness of $\ell = 5$ mm, using a power signal with a frequency of $\omega_\ell = 0.5$ rad s$^{-1}$. The thermal diffusion coefficient $D_s = 95 \cdot 10^{-6}$ m$^2$ s$^{-1}$, thermal conductivity $K_s = 200$ W m$^{-1}$ K$^{-1}$, and heat transfer coefficient $h = 60$ W m$^{-2}$ K$^{-1}$ values are taken from literature [39]. For the transmission mode, we observe within the laser spot radius, i.e., $\rho < a$, almost constant phase delay. The phase delay slope reaches the asymptotical value $-\rho/\lambda$ for $\rho \gg a$, as highlighted in [20]. On the other hand, in reflection mode, the phase delay is lower than in transmission mode in correspondence with the laser spot. However, the phase delay cannot be considered constant for $\rho < a$, as the curve slope quickly decreases. For $\rho \gg a$, the phase delays in both modes converge to the same value.

Similar considerations can be made on the gain of the transfer function (12), representing the temperature increase due to the input heat power. Fig. 4 shows an example of the magnitude behavior as a function of $\rho$, computed with the same physical parameters previously considered in the phase delay analysis. The magnitude values are normalized to the maximum achieved in reflection mode, corresponding to the laser spot center. In reflection mode, the temperature increase decays quite fast. Moving on the edges of the laser spot, we see less than 60% of the maximum temperature. In transmission mode, the maximum temperature increment is lower than the respective point on the other side of the sample. However, in correspondence to the laser spot, it is more constant. The temperature increment ranges from 54% to 43% for the center and the edge of the laser spot, respectively. Moving far from the laser spot, e.g., twice the radius, both surfaces have the same temperature increment, which decreases with the distance from the heat source. This behavior can be crucial in choosing the infrared camera to perform the data acquisition regarding sensor sensitivity. When measuring temperatures with a thermal camera across a wide temperature range, the impact of sensor noise is more significant in colder areas. In fact, colder areas emit less thermal radiation, resulting in a weaker signal reaching the camera's sensor. Moreover, the camera sensor introduces a constant level of noise, which becomes more significant relative to the weaker signal from colder objects. This lower SNR leads to a noisier image. From Fig. 4, we see that the wider temperature range is achieved in reflection mode, where the sensor noise may be relevant for analysis on large surfaces or small laser spot diameters.

## 3. Motivating applications

The ability to non destructively detect internal defects plays a crucial role in several fields. In particular, thermal process applications are more likely to be subjected to fatigue cracks. In this section, we provide some test case studies to show the applications of our testing technique.

Internal inhomogeneities in materials, such as porosity, inclusions, or microstructural defects, play a crucial role in corrosion behavior and, thus, in determining the efficiency of thermal processes [40]. For instance, in the battery case, internal defects prevent the thermal and electrical insulation and a high sealing level. The internal pores, often due to welding processes, are typically detected through expensive tests like X-ray or tomography (see, e.g., [41]). In this paper, we provide an efficient method for pores detection that can be implemented for in-line inspections.

Similarly, in heat exchangers, identified internal defects are associated with impaired heat transfer efficiency and increased thermal resistance. The ability to detect non-destructively material non-uniformities allows for timely maintenance and optimization of thermal systems, thereby enhancing energy efficiency and prolonging the lifespan of critical components [42]. Additionally, in additive manufacturing processes, detecting microstructural defects ensures the structural integrity and performance of 3D-printed parts, which is essential for their application in high-stress and high-temperature environments. The correlation between detected defects and their impact on thermophysical properties [43] highlights the importance of integrating advanced thermographic techniques in the quality assurance protocols of various

thermal engineering applications.

The effects of material properties and thermal cycles are studied in turbine rotors to investigate the thermal stresses (see, e.g., [44]). These studies involve finite element analysis methods and numerical models to account for thermal fatigue. However, these numerical studies do not consider pores in the material, often arising from production processes such as casting and welding. Still, they may introduce mechanical and thermal discontinuities, leading to failures. In [45], authors analyze the possibility of cracks in turbines operating in elevated temperature environments. Their study shows how subsurface cracks often start in proximity to casting pores. This highlights the importance of a non-destructive method for pore detection in high-reliability applications.

## 4. Thermal signal analysis

The thermal camera captures the temperature, either on the same side (reflection mode) $T(\rho,t) = T_s(\rho,0,t)$, or the opposite laser side of the specimen (transmission mode) $T(\rho,t) = T_s(\rho,\ell,t)$. The optical field of view is such that the observed area fully contains the corresponding region directly hit by the laser.

We denote by $T_k^{(r,c)}$ the 3D matrix arising from the thermal camera acquisition (see Fig. 5), where $k = 0,\dots,N-1$ are the discrete-time samples acquired at $t = k\ t_s$, $t_s = 1/f_s$ is the camera sampling time, $r = 1,\dots,H$ and $c = 1,\dots,W$ are row and column indexes, respectively, and the frame size is $H \times W$ pixels.

Given a single row-column index $(r^*,c^*)$ (e.g., the red pixel in Fig. 5), we get the 1-dimensional vector $T_k^{(r^*,c^*)}$, which contains the thermal behavior of the selected point. For the sake of simplicity in the notation, we omit the pixel index $(r,c)$ in the latter unless it is necessary for the algorithm, i.e., $T_k = T_k^{(r^*,c^*)}$. Fig. 6 shows a time-based profile of $T_k$ for a single pixel $(r^*,c^*)$ acquired during an experiment, where the specimen was thermally excited through a pulsed laser input acting at $f_\ell = 2$ Hz. The initial temperature $T_0$ is measured as the average value measured along the surface before switching on the laser. Thus, we get the temperature difference from the initial one as $\tau_k^{(r,c)} = T_k^{(r,c)}$.

We compute the oscillatory components of $\tau_k^{(r,c)}$ through the *Discrete Fourier Signal* (DFT) (see, e.g., [46]), which convert a uniformly sampled sequence of length $N$ into an equally-spaced sequence of the Fourier Transform. Given the sequence $\tau_k, k = 0,\dots,N-1$, the DFT is defined as

$$\tilde{\tau}_n = \sum_{k=0}^{N-1} \tau_k\ e^{-\frac{i2\pi nk}{N}} \in \mathbb{C},\ \forall n = 0,\dots,N-1. \tag{16}$$

The output is a sequence of $N$ complex numbers denoted by $\tilde{\tau}_n$, whose amplitude and phase are related to sinusoidal signals at frequency $f = n\ f_s/N$. The original signal $\tau_k$ can be retrieved through the linear combination of all the $N$ sinusoids defined by $\tilde{\tau}_n$.

**Remark 3.** To compute (16), the sampling time $k = 0$, i.e., $t = 0$, corresponds to the first laser pulse instant, and $k = (N-1)t_s$ is the last one.

Only $\tilde{\tau}_{n_\ell}$ for $n_\ell = N f_\ell/f_r$ is evaluated for all pixel index values $(r,c)$. We build the matrix $\tilde{\tau}^{(r,c)}$, which is the cartesian representation of $\tilde{\tau}_s(d,z)$ in (11). For each point $(r,c)$, we evaluate the phase of the complex number $\tilde{\tau}$

$$\angle\tilde{\tau} = \operatorname{atan2}\left(\mathbf{I}\left\{\tilde{\tau}\right\}, \mathbf{R}\left\{\tilde{\tau}\right\}\right), \tag{17}$$

where $\mathbf{R}\{\cdot\}$ and $\mathbf{I}\{\cdot\}$ are the argument real and imaginary part, respectively. $\operatorname{atan2}(y,x) \in [-\pi,\pi]$ is the angle measure between the positive $x$-axis and the ray joining the origin to the cartesian point $(x,y)$.

It is worth noting that $\tilde{\tau}_s(\rho,z)$, in (11), is derived for a uniform slab. On the other hand, $\angle\tilde{\tau}$ is derived from measurements performed on a defective part or, in general, a specimen to be inspected, e.g., a welding joint, which is not uniform in its composition. The specimen internal defects or nonuniformities act like an obstacle for the thermal waves, influencing the phase delay. In particular, while the input–output phase delay shows smooth changes along the radial component (see Fig. 3), large variations are expected in the presence of a nonuniform internal structure.

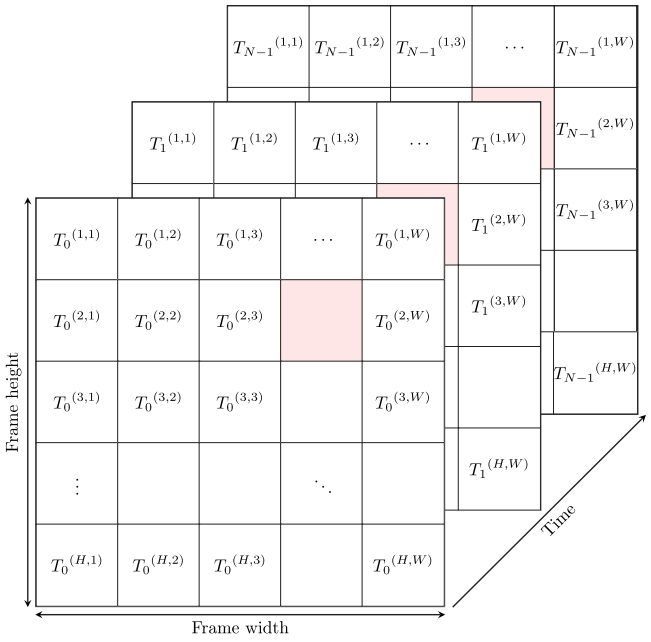


**Fig. 5.** Video data structure. $T_k^{r,c}$ represents the temperature of the pixel $(r,c)$ acquired at time $k$.

To highlight such variations, we exploit the numerical gradients along the two dimensions, row and column, i.e.,

$$\nabla\mathbf{F} = \frac{\partial\mathbf{F}^{(r,c)}}{\partial r}\vec{i} + \frac{\partial\mathbf{F}^{(r,c)}}{\partial c}\vec{j}, \tag{18}$$

where $\mathbf{F}$ is one among the amplitude $|\tilde{\tau}|$ or the phase matrix $\angle\tilde{\tau}$, and $\vec{i}$ and $\vec{j}$ and the versors along the row and column directions, respectively. The measure of the change rate is given from the element-wise gradient magnitude

$$|\nabla\mathbf{F}| = \left(\sqrt{\left(\frac{\partial\mathbf{F}^{(r,c)}}{\partial r}\right)^2 + \left(\frac{\partial\mathbf{F}^{(r,c)}}{\partial c}\right)^2}\right). \tag{19}$$

The matrix $|\nabla\mathbf{F}| \in \mathbb{R}^{H\times W}$ can be normalized to the maximum value and represented as a colored-value image. This image highlights the defects within the material, allowing, e.g., a non-experienced user, the material inspection. Unlike amplitude-based methods, which depend on absolute signal levels and may require complex normalization procedures, gradient magnitude is inherently independent of the signal module. High-gradient areas, indicative of discontinuities or edges, can be systematically identified, providing a robust foundation for automated defect detection algorithms.

The so-defined images that highlight defect contours can be used together with algorithms based on machine vision systems to recognize and classify defects.

In the latter, we present experimental testing results to show the efficiency of our approach.

## 5. Results and discussion

### 5.1. Experimental setup description

The thermographic testing employed laser-stimulated active thermography. The setup is a Multi-DES system for laser thermography testing and included a FLIR A6751sc IR thermal camera with a sensitivity below 20 mK, a Ytterbium pulsed fiber laser source producing

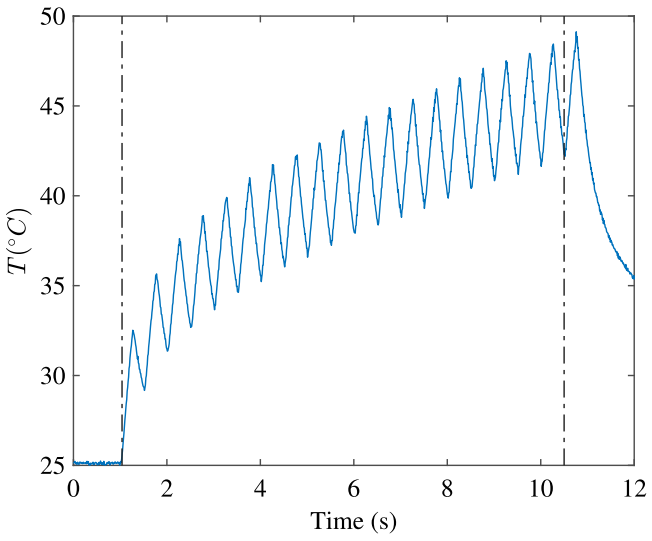


**Fig. 6.** Example of temperature signal acquired from the thermal camera for a single pixel. Dash-dotted lines represent the time of the first and the last temperature rise profile due to the laser impulses.

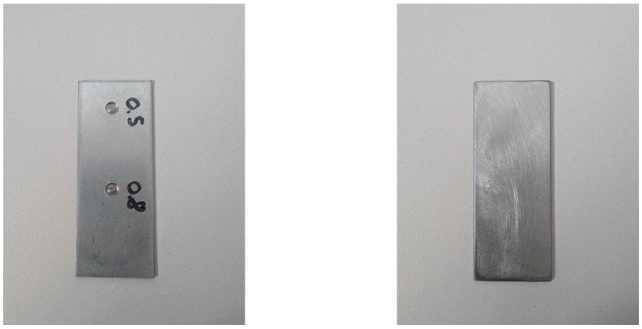


**Fig. 7.** Test plate used for experiment described in 5.2.

a maximum of 50 W power in an 8 mm diameter circular spot, and a PC control unit. We have run tests in both reflection and transmission modes, and the algorithm presented in Section 4 has been applied to detect defects through the generated images. Due to the thermal camera optical characteristics, we have set the distance between the thermal camera and the target equal to 420 mm, leading to 8 pixels per millimeter resolution.

### 5.2. Detecting holes on a metal plate

The first experiment we conducted was on a 1 mm thick DP600 steel plate, where two blind flat-top holes, 3 mm in diameter, have been drilled. The two holes, having depth 0.5 and 0.8 mm respectively, are placed on the same side, while the plate back is uniform (see Fig. 7).

The laser thermally excited the specimen, operating with a pulsed 7.5 W maximum power. We have chosen the modulation frequencies used in transmission and reflection modes from (15) such that the thermal diffusion length $\lambda$ is close to 0.5 mm, i.e., the half of the plate thickness, i.e., where the defect is likely to be positioned. Starting from $f_\ell = 3$ Hz, a fine parameter tuning procedure was performed through trial and error to highlight the defects better. The thermal camera was placed on the specimen back side such that the superficial defects on the front side do not affect the analysis results, and on the same side, in a more challenging application, to validate the methodology and showcase the usability for testing components where double side access is not assured. We repeated the experiments by focusing the laser on the two holes or the base material. We have generated the grayscale images for transmission and reflection configuration, shown in Figs. 8 and 9, respectively, through the algorithm described in the previous section.

We report the experimental results in transmission mode in Fig. 8. The tuned laser modulation frequency was $f_\ell = 4$ Hz. Concerning the theoretical analysis, we may expect round marks from the results of the proposed algorithm. However, in our experimental setup, the laser beam is not perpendicular to the specimen (see Fig. 1) since the laser source is at a lower height than the tested object. Thus, the thermal behavior may appear as an ellipsoid, especially while testing higher plate portions, due to the lack of an F-theta scan lens. However, in technical literature [47], it is common practice to use a laser beam angle with respect to surface normal lower than 20°. The experimental results are coherent with the theoretical analysis. The phase map diagrams, i.e., Figs. 8(a)–8(c), show that the maximum value (darker area) is reached where the laser is focused. Then, the phase decreases (lighter area) with increasing distance from the laser spot. It is worth noting that, from Figs. 8(a)–8(c), the presence of defects is unclear. On the other hand, by applying the proposed algorithm, the generated image from the phase gradient amplitude identifies the edges of the defects. While the testing on the base material, i.e., Fig. 8(e), produces a light gray mark, a darker mark is present on testing results when the laser is focused on the defective sections. Within the darker area in Figs. 8(d) and 8(f), a light circle is visible, corresponding to the defect. This is clear from the comparison between testing results and the plate picture (see Figs. 8(g)–8(i)), where the holes perfectly match the highlighted area.

For the test performed in reflection configuration (see Fig. 9), we tuned the laser excitation frequency $f_\ell = 5$ Hz. Also in this case, the phase map-based images are coherent with the theoretical results. Figs. 9(a)–9(c) show the maximum phase value in correspondence with the laser focus area (darker regions), and the phase decreases (brighter areas) with the distance from the laser spot. The images generated from the phase gradient magnitude allowed us to achieve a good contrast and find the hidden defects. The comparisons between the gradient phased-based images and the photo of the original plate (Figs. 9(g)–9(i)) show good matching between the highlighted area and the position of the holes.

The observed contrast maps in the images (Figs. 8 and 9) can be explained by the thermal behavior within the laser spot and its surroundings. In defect-free regions, the phase gradient tends to zero at the center of the laser spot, resulting in a brighter area with a smooth transition to the surrounding darker regions. This behavior is primarily due to uniform heat distribution in nominal conditions. However, the presence of a defect disrupts this uniformity, creating a localized and sharp transition between the darker and brighter areas. This sharper transition serves as a key indicator of defect presence.

To reliably detect defects, a defect-free region can serve as a reference for comparison. The smooth transitions observed in such regions can be used as a baseline to identify anomalies in areas with sharper transitions indicative of defects. Additionally, material properties such as thickness and thermal diffusion coefficients influence the sharpness of the transitions, which have been accounted for in the experimental analysis. This ensures that the proposed algorithm provides reliable results for identifying defects across various conditions and materials.

It is worth noting that, for the 0.8 mm deep hole, we get some different results from the 0.5 mm deep hole. In transmission mode (Fig. 8(f)), the surrounding gray circle is considerably smaller than in the other cases. On the other hand, in reflection mode (Fig. 9(f)), the deeper hole leads to a significant increase in the phase gradient magnitude, represented as a darker region. This is due to the thinner material left, 0.2 mm, which propagated the heat in a significantly different way from the 0.5 mm thick metal of the hole in Fig. 9(d). Once the defect is highlighted, it is possible to modify the excitation frequency to get a better image of the analyzed defect. Fig. 10(a) shows the testing results on the 0.8 mm deep hole in reflection mode with 10 Hz as excitation frequency.

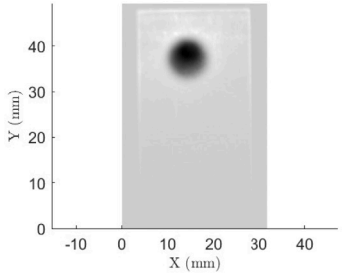


(a) Phase map diagram. The laser is focused on the $0.5\,\mathrm{mm}$ deep hole.

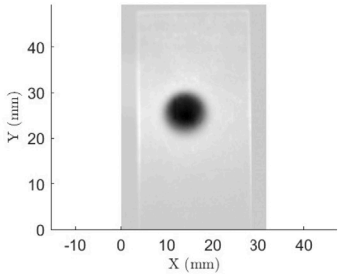


(b) Phase map diagram. The laser is focused on the base material.

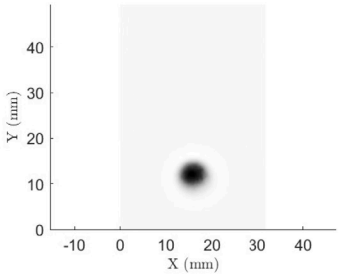


(c) Phase map diagram. The laser is focused on the $0.8\,\mathrm{mm}$ deep hole.

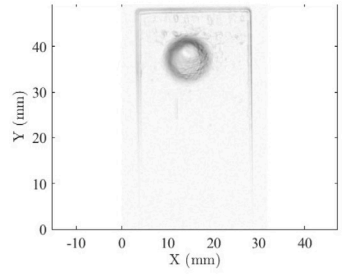


(d) Phase gradient magnitude map diagram. The laser is focused on the $0.5\,\mathrm{mm}$ deep hole.

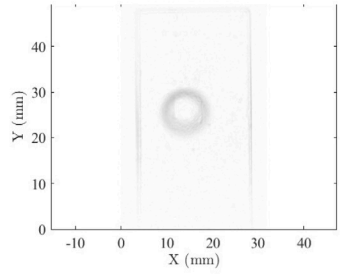


(e) Phase gradient magnitude map diagram. The laser is focused on the base material.

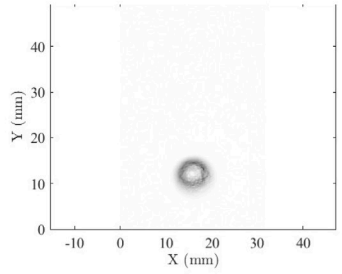


(f) Phase gradient magnitude map diagram. The laser is focused on the $0.8\,\mathrm{mm}$ deep hole.

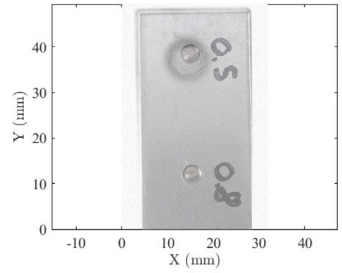


(g) Phase gradient magnitude map diagram, with the plate picture in overlay. The laser is focused on the $0.5\,\mathrm{mm}$ deep hole.

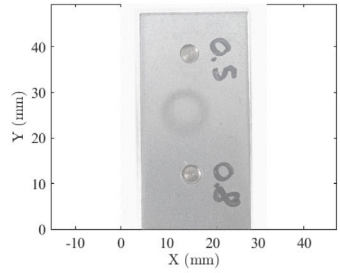


(h) Phase gradient magnitude map diagram, with the plate picture in overlay. The laser is focused on the base material.

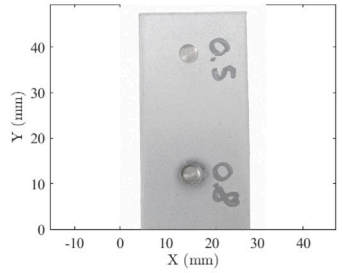


(i) Phase gradient magnitude map diagram, with the plate picture in overlay. The laser is focused on the $0.8\,\mathrm{mm}$ deep hole.

**Fig. 8.** Testing results of phase gradient magnitude in transmission mode for the experiment in Section 5.2. The analysis results are reported for the laser pointing to each plate hole and the base material. For each experiment, we report the phase map $\angle\tilde{\tau}$ (above), the phase gradient amplitude map $|\nabla\angle\tilde{\tau}|$, computed from (19), (middle row), and the phase gradient amplitude map with the plate pictured in the overlay (bottom) as a comparison. The images are generated in grayscale, where black represents higher values and white represents lower values.

### 5.3. Single plastic plate defect identification

This example employed a single 3D-printed plate fabricated from Polylactic Acid (PLA) to investigate defect identification methodologies. PLA was selected due to its widespread use in additive manufacturing, favorable mechanical properties, and ease of processing, which make it an ideal candidate for controlled defect studies. The plate was produced using a high-precision 3D printer, ensuring minimal material properties and geometry variability, crucial for accurate defect detection and analysis. To simulate hidden defects within the plate, we have divided the plate into $1 \times 1$ cm regions, where we have integrated a distinctive marker in the form of our laboratory's logo, "JTech", one letter for each region (see Fig. 11). The characters composing "JTech" are embedded within the plate at a depth of $0.5\,\mathrm{mm}$, ensuring that the defects are neither too superficial nor excessively deep, which could potentially affect the integrity of the plate or the detectability of the defects. The embedding process has been carefully controlled to maintain a consistent $1\,\mathrm{mm}$ plate thickness at the defect location, which is centrally positioned within the material to emulate real-world scenarios where defects may not always be on the surface. The tests are performed in reflection mode, where the laser is modulated at $f_\ell = 1$ Hz. We show the testing results in Figs. 12–13, where the colormap is grayscale with white for lower values and black for higher values.

Fig. 12 shows the analysis results achieved with the algorithm proposed. It is worth noting that the phase maps $\angle\tilde{\tau}^{(r,c)}$ alone do not provide a clear view of the internal defects, which are highlighted by the phase gradient maps $|\nabla\angle\tilde{\tau}|$. Still, the phase gradient method gives uncertain results on some letters of the "'JTech" logo, which may be better detected by fine-tuning the excitation frequency $f_\ell$. We have chosen to compare the results of the proposed technique on the

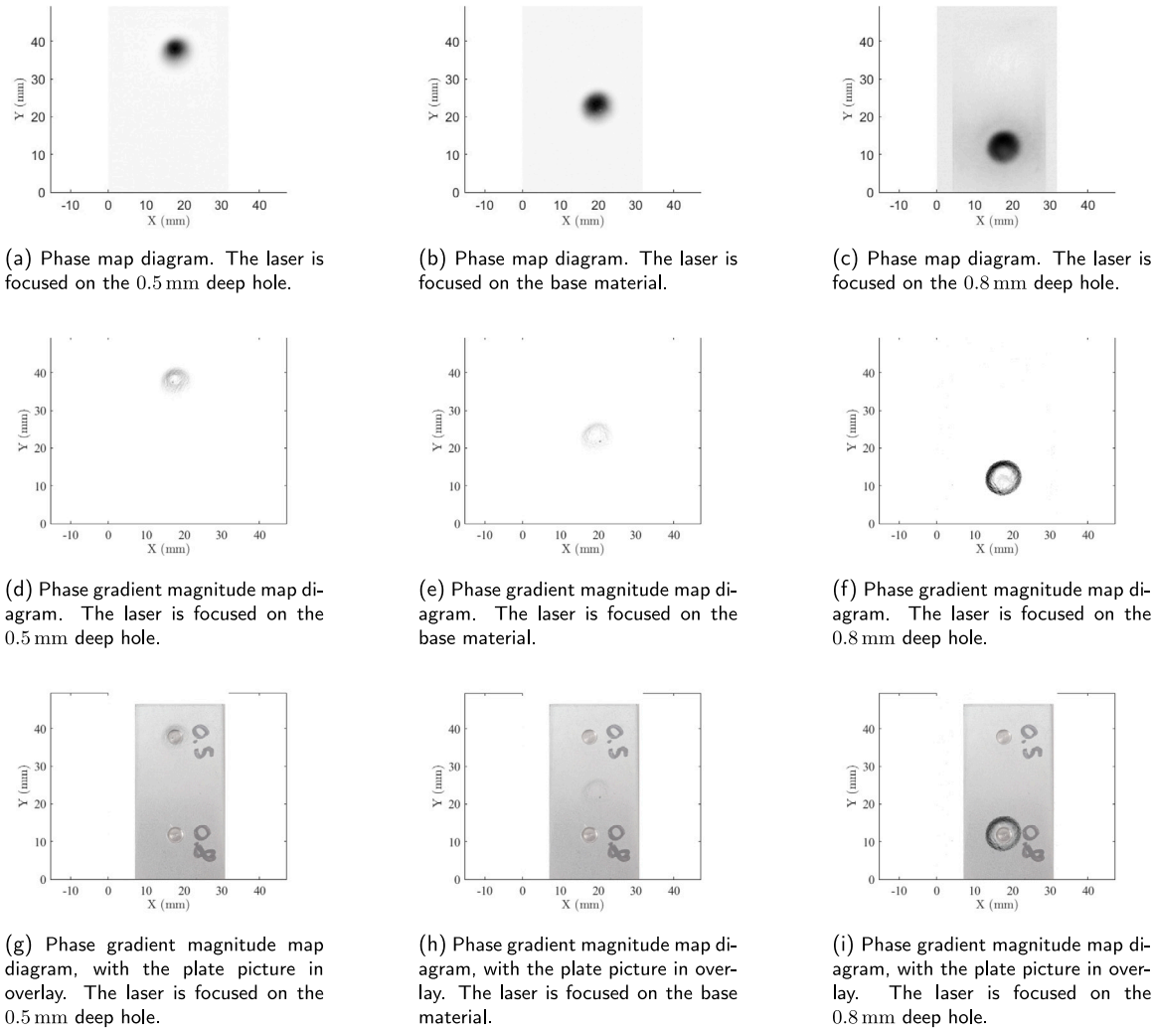


(a) Phase map diagram. The laser is focused on the $0.5\,\mathrm{mm}$ deep hole.

(b) Phase map diagram. The laser is focused on the base material.

(c) Phase map diagram. The laser is focused on the $0.8\,\mathrm{mm}$ deep hole.

(d) Phase gradient magnitude map diagram. The laser is focused on the $0.5\,\mathrm{mm}$ deep hole.

(e) Phase gradient magnitude map diagram. The laser is focused on the base material.

(f) Phase gradient magnitude map diagram. The laser is focused on the $0.8\,\mathrm{mm}$ deep hole.

(g) Phase gradient magnitude map diagram, with the plate picture in overlay. The laser is focused on the $0.5\,\mathrm{mm}$ deep hole.

(h) Phase gradient magnitude map diagram, with the plate picture in overlay. The laser is focused on the base material.

(i) Phase gradient magnitude map diagram, with the plate picture in overlay. The laser is focused on the $0.8\,\mathrm{mm}$ deep hole.

**Fig. 9.** Testing results of phase gradient magnitude in reflection mode for the experiment in Section 5.2. The analysis results are reported for the laser pointing to each plate hole and the base material. For each experiment, we report the phase map $\angle\tilde{\tau}$ (above), the phase gradient amplitude map $|\nabla\angle\tilde{\tau}|$, computed from (19), (middle row), and the phase gradient amplitude map with the plate pictured in the overlay (bottom) as a comparison. The images are generated in grayscale, where black represents higher values and white represents lower values.

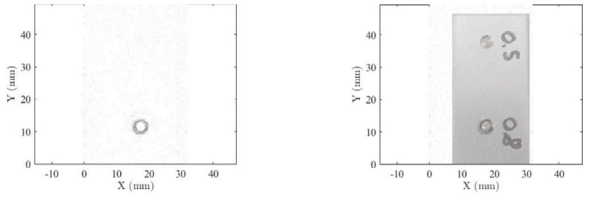


(a) Laser focused on 0.8 mm deep hole.

(b) Laser focused on 0.8 mm deep hole, with the plate pic in overlay.

**Fig. 10.** Testing result in reflection mode for the experiment in Section 5.2, where the excitation pulse frequency is set to 10 Hz. The analysis result is compared with the picture of the real defective plate in the figures in the bottom row.

**Fig. 11.** Single plastic plate — overview of embedded characters composing the writing word "JTech".

phase map to the amplitude map $|\tilde{\tau}^{(r,c)}|$. The amplitude map directly represents the signal intensity across the plate. In general, $|\tilde{\tau}^{(r,c)}|$ may include superficial defects due to the emissivity coefficient variation (see Remark 1). However, the testing plate was built purposely for this example through a 3D printer, and the surface was finely smoothed. Thus, we can assume the emissivity coefficient uniform along the specimen surface, giving us the possibility to compute the surface gradient on the module of $\tilde{\tau}^{(r,c)}$ to spot internal defects. Just like the proposed phase gradient magnitude matrix (19), the magnitude gradient map

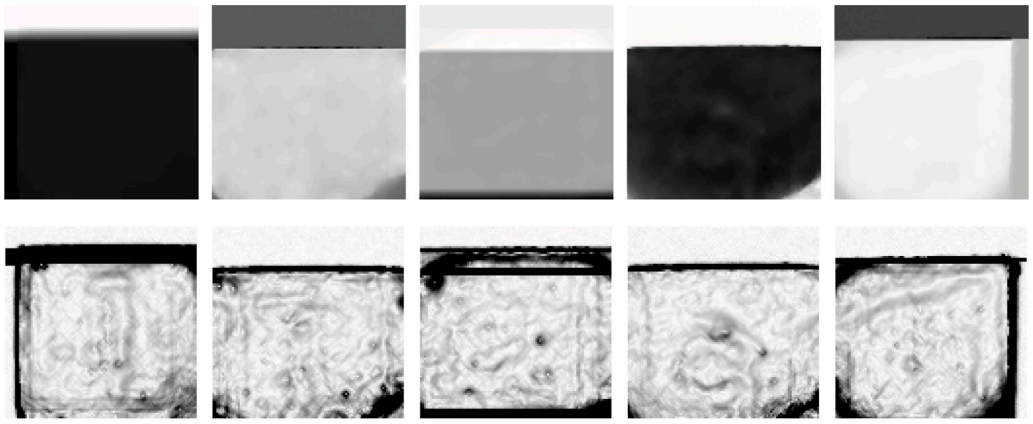

**Fig. 12.** "Jtech" test plate. On the top row, the phase map $\angle\tilde{\tau}^{(r,c)}$. On the bottom, the relative phase gradient map $|\nabla\angle\tilde{\tau}|$.

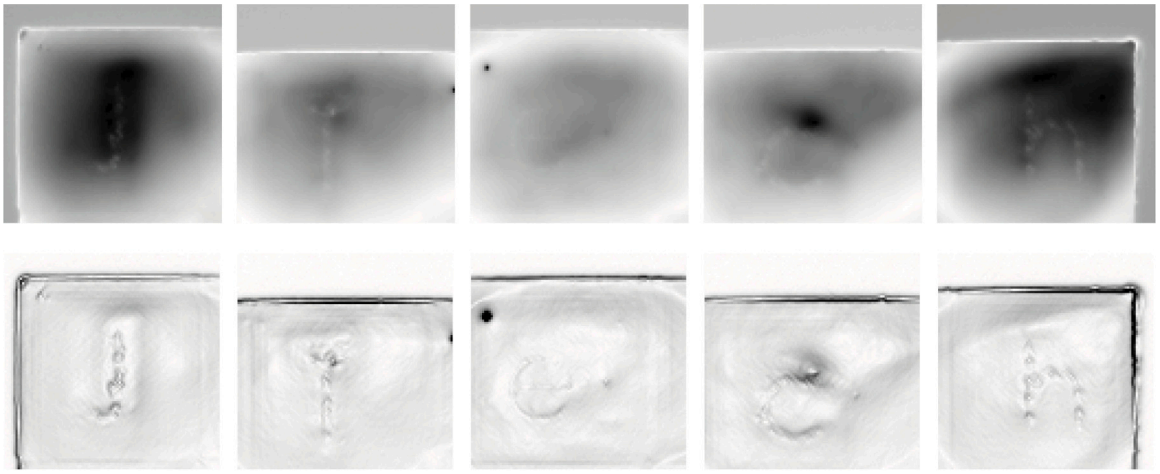

**Fig. 13.** "Jtech" test plate. On the top row, the amplitude map $|\tilde{\tau}^{(r,c)}|$. On the bottom, the amplitude gradient map $|\nabla|\tilde{\tau}||$.

offers a transformed representation where the focus is on the signal amplitude change rate. Fig. 13 compares the amplitude map $|\tilde{\tau}^{(r,c)}|$ with the proposed gradient-based generated image. The magnitude gradient maps clearly show the embedded "JTech" by accentuating the edges and boundaries of the defects, characterized by abrupt changes in material properties. The enhanced visibility of these features in the gradient map demonstrates its superior capability in highlighting subtle defects that may be overlooked in conventional amplitude mapping. The results from the amplitude map outperform the ones from the phase map, but they can be employed only in a few cases, i.e., when the emissivity coefficient is constant. It is worth noting that, through the gradient-based image generation technique, we do not need the exact knowledge of the emissivity coefficient during the thermal acquisition since it results in a scaling in the temperature measure, i.e., a constant offset while computing (19).

The improved contrast and clarity provided by the gradient magnitude map are particularly advantageous for distinguishing between actual defects and benign circular patterns that may arise from reflections or other lens imaging artifacts. This distinction is crucial for ensuring the accuracy of defect identification, as it reduces the likelihood of misclassification and enhances the reliability of the detection process.

## 6. Conclusion

This work has presented a rigorous and practical approach to non-destructive testing through gradient-based thermography. The methodology significantly enhances defect visualization by applying amplitude and phase gradient mapping, yielding superior contrast and precision in defect characterization compared to conventional techniques. The proposed algorithm provides a robust framework for accurately delineating defect dimensions and locations, underscoring its suitability for applications where material integrity is essential. Additionally, the potential for automation in defect detection suggests that this method could facilitate real-time inspection with notable efficiency. Future research may further refine this algorithm's adaptability to diverse material types and explore the integration of machine learning algorithms for more sophisticated defect classification.

It is demonstrated the pivotal role of internal inhomogeneities in influencing the efficiency and reliability of thermal processes. The gradient-based active thermography method presented herein proves to be a robust tool for the non-destructive detection and characterization of defects such as porosity and inclusions, which are critical factors affecting thermal conductivity, heat capacity, and thermal diffusivity. By accurately identifying these internal irregularities, the proposed methodology facilitates the optimization of thermal management systems, including battery thermal management, heat exchangers, and components produced through additive manufacturing. This advancement aligns with the broader objectives of improving energy optimization, reducing operational costs, and promoting sustainable practices in thermal engineering applications. Future research should explore the choice of suitable excitation frequencies to detect the presence of defects and to provide an accurate estimation of their position and size.

## Declaration of competing interest

The authors declare the following financial interests/personal relationships which may be considered as potential competing interests: Manuela De Maddis, Valentno Razza, Luca Santoro has patent #102023000023949 pending to Politecnico di Torino.

## Data availability

Data will be made available on request.

## References


[1] C. Meola, G.M. Carlomagno, L. Giorleo, The use of infrared thermography for materials characterization, J. Mater. Process. Technol. 155–156 (2004) 1132–1137, http://dx.doi.org/10.1016/j.jmatprotec.2004.04.268, Proceedings of the International Conference on Advances in Materials and Processing Technologies: Part 2.

[2] Q. Tang, J. Dai, C. Bu, L. Qi, D. Li, Experimental study on debonding defects detection in thermal barrier coating structure using infrared lock-in thermographic technique, Appl. Therm. Eng. 107 (2016) 463–468, http://dx.doi.org/10.1016/j.applthermaleng.2016.07.008.

[3] M.S. Carvalho, A.P. Martins, T.G. Santos, Simulation and validation of thermography inspection for components produced by additive manufacturing, Appl. Therm. Eng. 159 (2019) 113872, http://dx.doi.org/10.1016/j.applthermaleng.2019.113872.

[4] S. Doshvarpassand, C. Wu, X. Wang, An overview of corrosion defect characterization using active infrared thermography, Infrared Phys. Technol. 96 (2019) 366–389, http://dx.doi.org/10.1016/j.infrared.2018.12.006.

[5] E. Ichi, S. Dorafshan, Effectiveness of infrared thermography for delamination detection in reinforced concrete bridge decks, Autom. Constr. 142 (2022) 104523, http://dx.doi.org/10.1016/j.autcon.2022.104523.

[6] J.J. Faria, L.G. Fonseca, A.R. de Faria, A. Cantisano, T.N. Cunha, H. Jahed, J. Montesano, Determination of the fatigue behavior of mechanical components through infrared thermography, Eng. Fail. Anal. 134 (2022) 106018, http://dx.doi.org/10.1016/j.engfailanal.2021.106018.

[7] M. Inês Silva, E. Malitckii, T.G. Santos, P. Vilaça, Review of conventional and advanced non-destructive testing techniques for detection and characterization of small-scale defects, Prog. Mater. Sci. 138 (2023) 101155, http://dx.doi.org/10.1016/j.pmatsci.2023.101155.

[8] E. Barreira, R.M. Almeida, M. Moreira, An infrared thermography passive approach to assess the effect of leakage points in buildings, Energy Build. 140 (2017) 224–235, http://dx.doi.org/10.1016/j.enbuild.2017.02.009.

[9] M. Quercio, J.C. Del Pino Lopez, S. Grasso, A. Canova, Numerical and experimental analysis of thermal behaviour of high voltage power cable in unfilled ducts, Sci. Rep. 14 (1) (2024) 20599, http://dx.doi.org/10.1038/S41598-024-71281-X.

[10] A.N. Huda, S. Taib, Application of infrared thermography for predictive/preventive maintenance of thermal defect in electrical equipment, Appl. Therm. Eng. 61 (2) (2013) 220–227, http://dx.doi.org/10.1016/j.applthermaleng.2013.07.028.

[11] L. Giammichele, V. D'Alessandro, M. Falone, R. Ricci, Thermal behaviour assessment and electrical characterisation of a cylindrical Lithium-ion battery using infrared thermography, Appl. Therm. Eng. 205 (2022) 117974, http://dx.doi.org/10.1016/j.applthermaleng.2021.117974.

[12] H.A. Lauterbach, C.B. Koch, R. Hess, D. Eck, K. Schilling, A. Nüchter, The Eins3D project — Instantaneous UAV-Based 3D Mapping for Search and Rescue Applications, in: 2019 IEEE International Symposium on Safety, Security, and Rescue Robotics, SSRR, 2019, pp. 1–6, http://dx.doi.org/10.1109/SSRR.2019.8848972.

[13] Y. Zhou, P. Ghassemi, M. Chen, D. McBride, J.P. Casamento, T.J. Pfefer, Q. Wang, Clinical evaluation of fever-screening thermography: impact of consensus guidelines and facial measurement location, J. Biomed. Opt. 25 (9) (2020) 097002, http://dx.doi.org/10.1117/1.JBO.25.9.097002.

[14] J. Berce, M. Zupančič, M. Može, I. Golobič, Infrared thermography observations of crystallization fouling in a plate heat exchanger, Appl. Therm. Eng. 224 (2023) 120116, http://dx.doi.org/10.1016/j.applthermaleng.2023.120116.

[15] B. Ramzan, M.S. Malik, M. Martarelli, H.T. Ali, M. Yusuf, S. Ahmad, Pixel frequency based railroad surface flaw detection using active infrared thermography for Structural Health Monitoring, Case Stud. Therm. Eng. 27 (2021) 101234, http://dx.doi.org/10.1016/j.csite.2021.101234.

[16] Z. Omidi, S. Pozzer, X. Maldague, Integration of active thermography and ground penetrating radar for the detection and evaluation of delamination in concrete slabs, in: N.P. Avdelidis (Ed.), Thermosense: Thermal Infrared Applications XLV, Vol. 12536, SPIE, International Society for Optics and Photonics, 2023, p. 125360Y, http://dx.doi.org/10.1117/12.2664103.

[17] E. D'Accardi, D. Palumbo, R. Tamborrino, U. Galietti, A quantitative comparison among different algorithms for defects detection on aluminum with the pulsed thermography technique, Metals 8 (10) (2018) http://dx.doi.org/10.3390/met8100859.

[18] E. D'Accardi, A. Ulbricht, R. Krankenhagen, D. Palumbo, U. Galietti, Capability of active thermography to detect and localize pores in Metal Additive Manufacturing materials, IOP Conf. Series: Mater. Sci. Eng. 1038 (1) (2021) 012018, http://dx.doi.org/10.1088/1757-899X/1038/1/012018.

[19] M. Alhammad, N.P. Avdelidis, S. Deane, C. Ibarra-Castanedo, S. Pant, P. Nooralishahi, M. Ahmadi, M. Genest, A. Zolotas, L. Zanotti-Fragonara, J. Valdes, X.P.V. Maldague, Diagnosis of composite materials in aircraft applications: towards a UAV-based active thermography inspection approach, in: J.N. Zalameda, A. Mendioroz (Eds.), Thermosense: Thermal Infrared Applications XLIII, Vol. 11743, SPIE, International Society for Optics and Photonics, 2021, 1174306, http://dx.doi.org/10.1117/12.2586064.

[20] H. Kato, T. Baba, M. Okaji, Anisotropic thermal-diffusivity measurements by a new laser-spot-heating technique, Meas. Sci. Technol. 12 (12) (2001) 2074, http://dx.doi.org/10.1088/0957-0233/12/12/307.

[21] A. Mendioroz, R. Fuente-Dacal, E. Apiñaniz, A. Salazar, Thermal diffusivity measurements of thin plates and filaments using lock-in thermography, Rev. Sci. Instrum. 80 (7) (2009) 074904, http://dx.doi.org/10.1063/1.3176467.

[22] L. Santoro, M. Quercio, A. Canova, R. Sesana, Measuring thermal and electrical performances of additively manufactured magnetic shielding material: an active thermography approach, Nondestruct. Test. Eval. (2024) 1–24, http://dx.doi.org/10.1080/10589759.2024.2305703.

[23] T. Jaworski, P. Łuczak, J. Kucharski, Fuzzy logic based thermal image processing for temperature monitoring of rotating cylindrical surfaces, Appl. Therm. Eng. 254 (2024) 123793, http://dx.doi.org/10.1016/j.applthermaleng.2024.123793.

[24] R. Alfredo Osornio-Rios, J.A. Antonino-Daviu, R. de Jesus Romero-Troncoso, Recent Industrial Applications of Infrared Thermography: A Review, IEEE Trans. Ind. Inform. 15 (2) (2019) 615–625, http://dx.doi.org/10.1109/TII.2018.2884738.

[25] L. Santoro, R. Sesana, J. Diller, C. Radlbeck, M. Mensinger, Dissipative and thermal aspects in cyclic loading of additive manufactured AISI 316L, Eng. Fail. Anal. 163 (2024) 108446, http://dx.doi.org/10.1016/j.engfailanal.2024.108446.

[26] S. Bagavathiappan, B. Lahiri, T. Saravanan, J. Philip, T. Jayakumar, Infrared thermography for condition monitoring – A review, Infrared Phys. Technol. 60 (2013) 35–55, http://dx.doi.org/10.1016/j.infrared.2013.03.006.

[27] M. Quercio, E. Poskovic, F. Franchini, E. Fracchia, L. Ferraris, A. Canova, A. Tenconi, H. Tiismus, A. Kallaste, Application of active thermography for the study of losses in components produced by laser powder Bed fusion, J. Magn. Magn. Mater. 592 (2024) 171796, http://dx.doi.org/10.1016/j.jmmm.2024.171796.

[28] G. Dell'Avvocato, M. Rashkovets, A. Castellano, D. Palumbo, N. Contuzzi, G. Casalino, U. Galietti, Preliminary procedure for the assessment of probeless friction stir spot welds (P-FSSW) in dissimilar aluminum alloys by long pulsed laser thermography, in: F. López, N.P. Avdelidis, G. Ferrarini (Eds.), Thermosense: Thermal Infrared Applications XLVI, Vol. 13047, SPIE, International Society for Optics and Photonics, 2024, p. 130470R, http://dx.doi.org/10.1117/12.3013618.

[29] G. Dell'Avvocato, D. Palumbo, Thermographic procedure for the assessment of Resistance Projection Welds (RPW): Investigating parameters and mechanical performances, J. Adv. Join. Process. 9 (2024) 100177, http://dx.doi.org/10.1016/j.jajp.2023.100177.

[30] G. Dell'Avvocato, D. Palumbo, R. Pepe, U. Galietti, Non-destructive evaluation of resistance projection welded joints (RPW) by flash thermography, in: IOP Conference Series: Materials Science and Engineering, Vol. 1038, No. 1, 2021, 012003, http://dx.doi.org/10.1088/1757-899x/1038/1/012003.

[31] T. Sakagami, S. Kubo, Applications of pulse heating thermography and lock-in thermography to quantitative nondestructive evaluations, Infrared Phys. Technol. 43 (3) (2002) 211–218, http://dx.doi.org/10.1016/S1350-4495(02)00141-X.

[32] A. Choudhary, D. Goyal, S.S. Letha, Infrared thermography-based fault diagnosis of induction motor bearings using machine learning, IEEE Sensors J. 21 (2) (2021) 1727–1734, http://dx.doi.org/10.1109/JSEN.2020.3015868.

[33] T. Mian, A. Choudhary, S. Fatima, Multi-sensor fault diagnosis for misalignment and unbalance detection using machine learning, IEEE Trans. Ind. Appl. 59 (5) (2023) 5749–5759, http://dx.doi.org/10.1109/TIA.2023.3286833.

[34] H. Johnson, C. Burrus, On the structure of efficient DFT algorithms, IEEE Trans. Acoust. Speech Signal Process. 33 (1) (1985) 248–254, http://dx.doi.org/10.1109/TASSP.1985.1164526.

[35] L. Santoro, V. Razza, M. De Maddis, Frequency-based analysis of active laser thermography for spot weld quality assessment, Int. J. Adv. Manuf. Technol. 130 (5) (2024) 3017–3029, http://dx.doi.org/10.1007/s00170-023-12845-5.

[36] L. Santoro, V. Razza, M. De Maddis, Nugget and corona bond size measurement through active thermography and transfer learning model, Int. J. Adv. Manuf. Technol. 133 (11) (2024) 5883–5896, http://dx.doi.org/10.1007/s00170-024-14096-4.

[37] InfraTech GmbH, Quality assurance with active thermography in series test at Zwickau Volkswagen Plant, 2024, https://www.infratec-infrared.com/thermography/quality-assurance-with-active-thermography/. (Online; Accessed 24 December 2024).

[38] Urs Graf, Introduction to Hyperfunctions and Their Integral Transforms, Birkhäuser Basel, 2010, http://dx.doi.org/10.1007/978-3-0346-0408-6.
[39] E. MacCormack, A. Mandelis, M. Munidasa, B. Farahbakhsh, H. Sang, Measurements of the thermal diffusivity of aluminum using frequency-scanned, transient, and rate window photothermal radiometry. Theory and experiment, Int. J. Thermophys. 18 (1997) 221–250, http://dx.doi.org/10.1007/BF02575209.
[40] S. Du, M. Wang, S. Zhang, Z. Lv, Z. Xu, C. Liu, J. Wang, J. Liu, B. Liu, Effect of micron-sized inclusions on the corrosion behavior of recycled Al-Zn-Mg-Cu alloy sheet, Mater. Charact. 218 (2024) 114517, http://dx.doi.org/10.1016/J.MATCHAR.2024.114517.
[41] M. Orlando, M. De Maddis, V. Razza, V. Lunetto, Non-destructive detection and analysis of weld defects in dissimilar pulsed GMAW and FSW joints of aluminium castings and plates through 3D X-ray computed tomography, Int. J. Adv. Manuf. Technol. 132 (2024) 2957–2970, http://dx.doi.org/10.1007/s00170-024-13576-x.
[42] I. Orynyak, M. Zarazovskii, M. Borodii, A new methodology for structural reliability assessment of the heat exchanger tubes of WWER steam generators, J. Press. Vessel. Technol. 139 (3) (2017).
[43] M. Quercio, L. Santoro, E. Poskovic, R. Sesana, A. Canova, Magnetic and thermal characterization of Fe2.9wt.%Si for magnetic shielding applications, IEEE Access (2024) 2890–2902, http://dx.doi.org/10.1109/ACCESS.2024.3524238.
[44] M. Banaszkiewicz, On-line monitoring and control of thermal stresses in steam turbine rotors, Appl. Therm. Eng. 94 (2016) 763–776, http://dx.doi.org/10.1016/j.applthermaleng.2015.10.131.
[45] X. Li, W. Li, M. Imran Lashari, T. Sakai, P. Wang, L. Cai, X. Ding, U. Hamid, Fatigue failure behavior and strength prediction of nickel-based superalloy for turbine blade at elevated temperature, Eng. Fail. Anal. 136 (2022) 106191, http://dx.doi.org/10.1016/j.engfailanal.2022.106191.
[46] R.L. Allen, D.W. Mills, Signal Analysis: Time, Frequency, Scale, and Structure, John Wiley & Sons, 2004, http://dx.doi.org/10.1002/047166037X.
[47] G. Dell'Avvocato, D. Palumbo, U. Galietti, A non-destructive thermographic procedure for the evaluation of heat treatment in Usibor®1500 through the thermal diffusivity measurement, NDT & E Int. 133 (2023) 102748, http://dx.doi.org/10.1016/j.ndteint.2022.102748.